Materials Today Bio 28 (2024) 101224

Contents lists available at ScienceDirect

Materials Today Bio

journal homepage: www.journals.elsevier.com/materials-today-bio

Flexible and high-strength bioactive glass fiber membrane for bone regeneration with the aid of alkoxysilane sol spinnability

Junjie Mao [a,1], Junyuan Sun [b,1], Lu Wang [a], Xinyu Liu [b,*], Jianqiang Bi [a,**]

[a] Liquid-Solid Structural Evolution & Processing of Materials (Ministry of Education), School of Materials Science and Engineering, Shandong University, Jinan, Shandong, 250061, PR China
[b] Department of Orthopaedics, Qilu Hospital of Shandong University, Jinan, Shandong, 250012, PR China

ARTICLE INFO

Keywords:
Bioactive glass fiber membranes
Alkoxysilane sol
Chain-like polysiloxane
Electrospinning
Mechanical properties
Osteogenesis

ABSTRACT

In this research, the spinnability of bioactive glass (BG) precursor solution was supplied by alkoxysilane sol with appropriate molar ratio of H_2O/silicon (R) to prepare bioactive glass fiber membrane (BFM) using electrospinning (ES) technique. Alkoxysilane could form a linear or chain-like colloidal aggregation in hydrolysis-polycondensation with R = 2 or so, thereby exhibiting good spinnability. Therefore, the role of polymer binders could be largely replaced. Due to the significant decrease of polymer binder, the defects within the fibers are largely reduced and degree of fiber densification was improved after calcination, leading to BFM drastically enhanced strength and flexibility. The effect of R and calcination temperature on mechanical performance were investigated in detail. The tensile strength could reach the highest value 2.31 MPa with R = 2 and calcination at 700 °C. In addition, under this preparation condition, the BFM also possessed good flexibility with bending rigidity 37.7 mN. Furthermore, the great performance of promoting cell proliferation and osteogenesis could be observed from *in vitro* cellular experiment. The BFM calcined at 750 °C exhibited the best promoting osteogenic differentiation ability. The rat skull defect model revealed BFM could perform well in osteogenesis *in vivo*.

1. Introduction

Bone repair and reconstruction in both orthopaedic and dental renovations are still confronted with various challenges, although much progress has been made in the past forty years [1–3]. Modern medicine is committed to designing biomaterials with possess controllable resorption and the capability of inducing tissue regeneration. An important example is osteogenic biomaterials, conventionally termed "scaffolds", which have been gaining wide attention [4,5]. Typically, 3D bioceramic scaffolds such as hydroxyapatite (HA), tricalcium phosphate (TCP), and bioactive glass (BG) face significant challenges in clinical applications due to their inferior mechanical properties compared to natural bone [6,7]. This limitation stems from the inherent brittleness of ceramic materials, which results in considerably lower tensile strength and fracture toughness than those required for applications [8]. Consequently, in the current form as 3D scaffolds, bioceramic is unsuitable for primary load-bearing applications. What's more, scaffolds fabricated using methods such as 3D printing or foam replication typically exhibit relatively large pore sizes (generally greater than 100 μm), which may not promote cellular adhesion and penetration into the scaffold's interior [9,10]. Furthermore, sintered bioceramics often possess high density, which significantly diminishes their bioactivity after implanted *in vivo* [11].

Bone extracellular matrix (ECM) secreted by osteoblasts is constituted of collagen fibrils and mineralized apatite [12]. An excellent bone scaffold should imitate the fibrous structure of the ECM [13]. Electrospinning (ES) is an effective technique for manufacturing continuous and high-quality fibers with diameters ranging from nanometer to micrometer, which is beneficial for mimicking the structure of ECM [14]. ES fibers have been applied for drug delivery, biological dressings and enzyme immobilization [15]. ES for BG fibers derived from sol–gel solution is becoming ever-increasingly widespread. Weng et al. [16] fabrication of strontium (Sr) and copper (Cu) doped BG nanofibers by electrospinning followed by a post processing heat treatment to remove the polymer. *In vitro* cell culture studies testified Sr dopant significantly enhanced osteogenesis and suppressed osteoclastogenesis, while

* Corresponding author.
** Corresponding author.
E-mail addresses: 200262000203@sdu.edu.cn (X. Liu), bjq1969@sdu.edu.cn (J. Bi).
[1] Junjie Mao and Junyuan Sun contributed equally to this work.

https://doi.org/10.1016/j.mtbio.2024.101224
Received 1 June 2024; Received in revised form 25 August 2024; Accepted 1 September 2024
Available online 4 September 2024

meanwhile, Cu dopant promoted the angiogenesis. Chen et al. [17] synthesized by combining L-Buthionine sulfoxide (BSO) loaded tannic acid (TA)/Fe^{3+} nanoparticles and vascular endothelial growth factor loaded electrospun BG fibers. The implantable system possessed excellent anti-tumor and tissue regeneration function. Most of above these researches certainly didn't apply electrospun BG fiber sample as a membrane scaffold but just powder or stuffer because of the weak mechanical performance (low strength and brittleness). And few studies on the mechanical properties of the bioactive glass fiber membrane (BFM) have been reported.

In comparison, the ES fiber membranes of biocompatible polymer including PLA, PCL and gelatin have been widely used as biological dressings and tissue repair on account of its good practicability and compatibility [18,19]. There are two main reasons causing such big gap between BFM and polymer fiber membrane. One is because the inherent brittleness of ceramics such as BG conflicts with the flexibility and stretchability needs of membrane scaffolds. Moreover, since nearly all electrospun BG fibers derived from sol-gel solutions are obtained with the aid of polymer binders, the elimination of organic component at high temperatures leads to mechanical properties deterioration and embrittlement [12,20]. The mechanical properties of BG are crucial for the practical application of flexible BFM. The improvement can be achieved from the second point, now that the first can hardly be changed. Seeking a method to reduce the polymer binder without affecting the ES process is the key to solving this problem.

Previous researches on BG non-woven membranes need sufficient addition of polymer binder to produce continuous fibers. The viscosity increase mainly relies on the entanglement and chain overlap between polymer molecules. The intermolecular forces (e.g., hydrogen bonding) between alkoxysilane after hydrolysis-polycondensation is often neglected [21,22]. Sakka et al. [23,24] reported a ES process of silica (SiO_2) fiber, using tetraethyl orthosilicate (TEOS, a kind of alkoxysilane)/ethanol/H_2O/hydrochloric acid (HCl) reaction system, when the R is about 2 under appropriate acidic environment. The hydrolysis and condensation of TEOS lead to linear or chain-like polysiloxane (Scheme 1) and consequently great spinnability without polymer binder. Larger R values (>4) cause the formation of non-linear SiO_2 network structure. It can be seen from Sakka's work that the interaction between linear or chain-like polysiloxane is enough to support the continuous stretching of jet in pure SiO_2 system. However, for BG sol system electrospinning, the introduction of Ca^{2+} increases the charge density of the jet, which causes the great increase of conductivity and repulsive force within the jet. Poologasundarampillai et al. [25] tried to prepared electrospun BG fibers without polymer. Only 3D scaffolds composed of "cotton-wool" short fiber was obtained, because the introduction of Ca^{2+} caused the stretching increase and wet jet breakup. Therefore, glass precursor solutions with lower viscoelasticity still need a small amount of high molar mass polymers to avoid splitting and instability due to the repulsion.

In this work, we prepared the BFM with a unique method that was different from previous researches. We improved the spinnability of the bioactive glass sol greatly by utilizing the alkoxysilane under an appropriate condition hydrolysis-condensation (i.e., R = 2 or so). This specific water content caused the formation of linear or chain-like colloidal aggregation in hydrolysis-polycondensation, thereby exhibiting good spinnability. Therefore, the role of polymer binders could be largely replaced. What's more, due to the high concentration ions (such as Ca^{2+}) in the concentrated BG sol, a very small amount of the specific polymer binder still needed to be added to resist repulsive force and avoid fiber breakage in this system. Due to the amount of polymer largely decreased, the defects of the fibers caused by polymers removal after calcination were greatly reduced and the fibers densification degree was improved, so that BFM with flexibility and high strength was obtained. It was capable of conforming to bone defects of any shape while maintaining a lower stiffness to prevent undue pressure on surrounding tissues. In contrast to bioceramic high density bulk or scaffold with large pore size (>100 μm), the microscopic texture of fibrous membranes facilitates intimate material and information exchange with

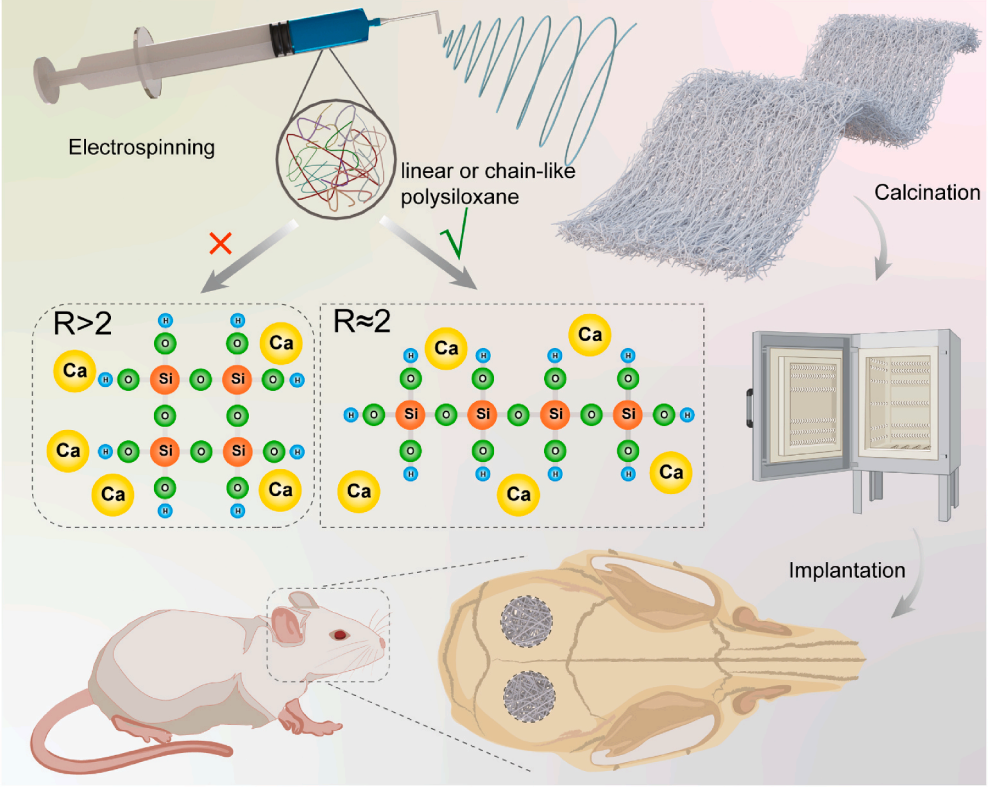

Scheme 1. Schematic illustration of the construction of bioactive glass membranes and the bone defect therapy.

the biological system. This endows it with better capabilities for ion release, induced mineral deposition and cellular adhesion. Furthermore, the great performance of promoting cell proliferation and osteogenic differentiation could be observed from *in vitro* cellular experiment. The rat skull defect model revealed BFM could perform well in osteogenesis *in vivo*.

2. Experiments

2.1. Fabrication of BFM

The BFM (Si/Ca molar ratio: 85/15) were fabricated upon sol-gel method. Firstly, 1.31 g $CaCl_2$ was dissolved in 7 mL ethanol, then 15 mL TEOS was added. After stirring for half hour, the solution was added with different amounts of H_2O (R = 1.8, 2.0, 2.2 and 2.4). Subsequently, 100 μL HCl (1N) was added into the above solution and stirring continued another 2 h. Afterwards, 0.12 g PVP (MW:1,300,000) was added into the sols. The obtained sols were stirred for 36 h under ice bath conditions, while persistent volatilization to increase the viscosity of the sols. The aged hybrid solutions were loaded in plastic syringes equipped with a metallic needle (21 gauge) to spin the fiber. The high tension field (12 kV) was adopted to the metal needle and a plate collector. The obtained precursor of bioactive glass membrane (PBFM) were transferred into the oven at 60 °C for 24 h to volatilize the residual solvents. The PBFM obtained was denoted PBFM-R value, for example PBFM-2.0. Finally, the PBFMs were heated up to specific temperatures (600, 650, 700, 750, 800 °C) with a heating rate of 1 °C/min and annealed at the corresponding temperature for 5 h in air. The BFM obtained was denoted BFM-R value-calcination temperature, for example BFM-2.0-700. For precursor of SiO_2 fiber membrane (PSFM), due to the absence of highly conductive phase calcium ions, the spinnability can be accomplished easily without high polymer provided R approximate 2.0. So the PSFM was prepared in a similar way with PBFM but not adding PVP and R equal to 2.0. And SiO_2 fiber membrane (SFM) was obtained by calcination at 600 °C.

2.2. Characterization

The morphology and elemental compositions of BFMs were investigated using the field scanning electron microscopy (FE-SEM, JSM-7800, 20 kV) with an energy dispersive X-ray spectroscopy (EDS). The phase compositions were measured by X-ray diffraction (XRD, D/MAX-Ultima IV, Rigaku, Japan). Weight loss and possible phase transition during calcination of PBFM and PSFM were measured using thermogravimetry and differential scanning calorimetry (TG-DSC, TGA/DSC 3+, LER TOLEDO, Switzerland) at a heating rate of 10 °C/min. The functional groups and chemical structure of PBFMs and PSFM were examined using Fourier-transform infrared spectroscopy (FTIR, Nicolet IS50, Thermo Scientific, USA). The Si-O network structure of the BFMs was tested by Raman spectroscopy (LabRAM HR evolution, Jobin Yvon-Horiba, France) over the 50-2500 cm^{-1} range. The Attenuated Total Reflection Fourier transform infrared spectroscopy (ATR-FTIR) was applied to BFMs to detect the bond of Si-O. The chemical state of Calcium element was analyzed by X-ray photoelectron spectrometer (XPS, scientific-LabRAM HR evolution, Horiba, Japan). The Ca^{2+} release of the BFMs was measured by Ca^{2+} colorimetric assay kit (elabscience, china) as follows: 0.5 g of BFMs was soaked in 100 mL of phosphate buffered saline (PBS), half of PBS was removed at specific time points (1, 3, 5, 7, 10, 14, 21 and 28 days) for assay analysis to determine the concentration of Ca in the PBS, and equivalent fresh PBS was added to the immersed samples.

2.3. Mechanical properties tests

Tensile strength of BFMs was analyzed using an electronic fiber strength tester (LLY-06). The strength of BFMs with a thickness of 50 ± 10 μm and size of 10 mm * 5 mm was measured [26]. And softness was evaluated with a softness analyzer (RRY-1000, Hangzhou Qingtong & Boke Automation Technology Co., Ltd., China). The tensile strength of BFM-2.0-700 was also measured after different degradation time (0, 7, 14, 21, 28 days, 0 day referred to testing immediately after soaking). The softness of BFMs with a thickness of 55 ± 8 μm and size of 10 cm × 10 cm was measured with the ASTM D2923-95 test [27].

2.4. Biomineralization experiments in vitro

Simulated body fluid (SBF) was prepared according to the usual procedure [28] given using chemicals purchased from Sinopharm Chem. Reagents Co Ltd. The bioactivity of BFMs calcined at different temperature were tested *in vitro* through immersing sample fragments in SBF at 37 °C to monitor the formation of hydroxycarbonate apatite (HCA) for different time intervals (3, 5, 7 days). The biomineralization behavior of BFMs was analyzed using SEM and FTIR.

2.5. Cell proliferation on BFMs

In order to research the effect of heat treatment on evaluate cell activity, MC3T3-E1 cells were cultured on BFMs calcined at different temperature and SFM as control. Cell activity and proliferation were determined by cell counting kit-8 (CCK-8) assay. Prior to seeding cells, a 12 mm circular BFM was placed into each well of a 48-well plate 4 h in advance. After digesting the cells, 1 mL cell suspension (5×10^3 cells/mL) was added into each membrane and cultured with culture medium (α-minimum essential medium, 1 % penicillin/streptomycin, and 10 % fetal bovine serum) for periods from 1 to 7 days. At different culture time points (1, 4 and 7 days), CCK-8 was mixed with culture medium in a volume ratio of 10 %. After 4 h incubation, 100 μl the mixed solution was transferred into a 96-well plate to measure the absorbance at 450 nm using a microplate reader (Thermo Labsystems, America). The viability of MC3T3-E1 in the scaffolds was measured by the calcein AM (Beyotime, China). The samples containing cells were washed with PBS 3 times and treated with calcein AM for 30 min at 37 °C. Cells on the membranes were observed under the inverted fluorescent microscope (Zeiss, Germany) in a dark environment.

2.6. Cell adhesion on BFMs

Confocal laser scanning microscope (CLSM, Andor, UK) and SEM were used to characterize the adhesion and morphology of MC3T3-E1 on SFM and BFMs. For CLSM observation, after culturing for 4 days, the samples were washed 3 times with PBS for 5 min each time. The cells were fixed with 4 % PFA for 30 min at 4 °C. The fixed cells were then stained with FITC-phalloidin to mark the F-actin and DAPI to mark the nucleus. After staining, the adhesion and morphology of MC3T3-E1 were observed using CLSM. For SEM observation, after culturing for 4 days, the SFM and BFMs were washed 3 times with PBS for 5 min each time. The cells on membranes were fixed with 4 % PFA for 25 min at 4 °C. Then the cells were dehydrated with gradient ethanol (5 %, 10 %, 15 %, 20 %, 30 %, 50 %, 75 %, 80 %, 95 %, 100 %) 10min for each time, and dried using the hexamethyldisilazane (HMDS) drying method. Finally, cell adhesion and morphology was observed with SEM.

2.7. Gene expression of cells on BFMs

To evaluate the effect of heat treatment on osteogenic differentiation, reverse transcription-polymerase chain reaction (RT-PCR) was employed to evaluate it at the mRNA level. After 7 days culturing on BFMs, 4 osteogenic–related genes including Runt-related transcription factor 2(*RUNX2*), alkaline phosphatase (*ALP*), collagen type I (*COL1*) and osteocalcin (*OCN*) were detected, while glyceraldehyde-3phosphate dehydrogenase (*GAPDH*) was adopted as the reference gene to normalize target gene expression levels. SFM which was set as the

control group were also seeded and detected. At point of 7 days, the cells were digested from samples with trypsin, then centrifuged and collected. Messenger RNA (mRNA) was extracted from the cells using the RNA extraction kit. Afterwards, mRNA was reverse transcribed into complementary DNA (cDNA) by using the ReverTra Ace qPCR RT kit (TOYOBO, Japan). Finally, SYBR Green Realtime PCR Master Mix (TOYOBO, Japan), the primers and the cDNA were mixed together. RT-PCR was performed to reveal any fold changes in the expression of targeted genes on BFMs compared to SFM as control.

2.8. Immunofluorescence (IF) staining of cells on BFMs

The expression of osteogenic differentiation-related proteins was detected by IF staining. After culturing MC3T3-E1 on SFM and BFMs for 14 days, the medium in wells was removed and the cells-membranes complexes were fixed using 4 % PFA for 30 min. Subsequently, the complexes were permeabilized with 0.1 % Triton X-100 (Solarbio, China) and blocked with 5 % bovine serum albumin (BSA, Solarbio, China) blocking buffer. The samples were divided into two groups. Respectively, each group complexes were incubated with OCN Polyclonal antibody (Proteintech, China) and COL1 Polyclonal antibody (Proteintech, China) overnight at 4 °C and the CoraLite 488-conjugated secondary antibody (Proteintech, China) for 1 h. Finally, the complexes were stained with TRITC-Phalloidin (Solarbio, China) and DAPI. PBS washing was required 3 times after each procedure. The complexes were investigated using CLSM with 405 mm (blue fluorophore), 488 mm (green fluorophore) and 561 mm (red fluorophore) wavelengths, for DAPI, proteins and F-actin, respectively. The mean gray value of the targeted protein was measured using Image J.

2.9. Western-blot (WB) assays

After culturing MC3T3-E1 on SFM and BFMs for 14 days, RIPA lysis buffer including protease inhibitors (Sigma-Aldrich, USA) was used to lyse the MC3T3-E1 cells. Then, the solution was centrifuged at 12,000 rpm at 4 °C for 15 min. SDS-PAGE was used to separate proteins at 100V. Then proteins were transferred onto 0.22 μm polyvinylidene fluoride membranes (Millipore, USA) at 300 mA. 5 % skimmed milk powder solution was used to block the membranes at room temperature for 60 min. Then the membranes were treated with the following primary antibodies at 4 °C overnight: ALP (1:1000, Abcam), RUNX2 (1:1000; Cell Signaling Technology), OPN (1:1000, Affinity), COL1 (1:1000, Proteintech). Finally, the membranes were incubated with secondary antibody (1:2000, Proteintech) at room temperature for 1 h. An enhanced chemiluminescence kit (Millipore, USA) was applied to detect the membranes. Protein contents were quantified by Image J software.

2.10. ALP staining and alizarin red S (ARS) staining of cells with BFMs leach liquor

For ALP staining and ARS assays, the condition medium was prepared by soaking SFM and BFMs in inductive medium (5 mg/mL) to induce osteogenic differentiation of MC3T3-E1. For ALP staining, the cells were fixed with 4 % PFA for 30 min and stained with BCIP/NBT Alkaline Phosphatase Color Development Kit (Beyotime, China). For ARS assay, cells were fixed with 4 % PFA and stained with ARS Staining Kit (Beyotime, China) for 30 min. The excess ARS stain was removed and cells were washed 3 times using deionized water. Images were captured using an optical microscope. In a quantitative analysis for ARS, the stain was dissolved in 1 mL 10 % cetylpyridinium chloride (Macklin, China) solution for 30 min, and the absorbance of the obtained solution was measured at a wavelength of 562 nm on the microplate reader.

2.11. In vivo bone regeneration study

Animal experiments were approved by the Laboratory Animal Ethical and Welfare Committee of Shandong University Cheeloo College of Medicine. Male Sprague-Dawley(SD) rats (8 weeks) were supplied by Beijing Vital River Laboratory Animal Technology Company and raised in a specific pathogen-free (SPF) environment with a 12 h light–dark cycle. In this study, rat cranial defect model was used to assess bone regeneration. The membranes were cut into 4 mm diameter discs and sterilized using UV irradiation, then washed and soaked in 10 % penicillin/streptomycin PBS for 24 h. 15 rats were divided into three groups: control group (CN), SFM group and BFM-2.0-750 group. After anesthesia with isoflurane, the rats were placed in a stereotaxic frame and fixed during surgery. The hair on the skull was shaved off, and then a surgical incision was made along the midline from the nasofrontal lobe to the occipital region to expose the skull. A PBS-cooled stainless steel ring drill (4 mm diameter) was used to remove the full layer of bone and create a 4-mm defect on both sides of the dorsal aspect of the skull for membrane implantation.

After 8 weeks, rats were executed and their skulls were collected and fixed in 4 % paraformaldehyde for Micro-CT (Quantum GX2, PerkinElmer, Japan) analysis. Scanning parameters were set to a source voltage of 90 kV, a source current of 88 μA, and a scanning slice thickness of 7 μm. Three-dimensional (3D) images, bone volume (BV)/tissue volume (TV) ratios, trabecular separation (TB.N) and bone mineral densitywere (BMD) were reconstructed and analyzed. Afterwards, these samples were decalcified in EDTA-Na2 and then embedded in paraffin for sectioning and subjected to hematoxylin-eosin (HE), Masson's trichrome staining and immunohistochemistry.

2.12. Statistical analysis

Data were expressed as the mean ± standard deviation from at least three independent experiments. Differences among groups were analyzed by ANOVA (SPSS Statistics 26). $\forall P < 0.05$, $\forall\forall P < 0.01$ and $\forall\forall\forall P < 0.001$ compared with the first group in chart. $\#P < 0.05$, $\#\#P < 0.01$ and $\#\#\#P < 0.001$compared with the second group in chart. $\ni P < 0.05$, $\ni\ni P < 0.01$ and $\ni\ni\ni P < 0.001$ compared with the third group in chart. $^{*}P < 0.05$, $^{**}P < 0.01$ and $^{**}P < 0.001$ compared with the fourth group in chart. $\Delta P < 0.05$, $\Delta\Delta P < 0.01$ and $\Delta\Delta\Delta P < 0.001$ compared with the fifth group in chart. $\Phi P<0.05$, $\Phi\Phi P<0.01$ and $\Phi\Phi\Phi P<0.001$ compared with the sixth group in chart.

3. Result and discussion

3.1. Morphology and phase composition analysis

The electrospinning ability depends on the specific components during the BFM precursor solutions setting. Due to the high concentration polysiloxane and Ca^{2+} of the sol, the polymer dissolution would become extremely hard, in which the choice of calcium source played a vital role. As shown in Fig. S1a, the combinations of PVP + $Ca(NO_3)_2$ or Polyvinyl Butyral (PVB) + $CaCl_2$ couldn't form the uniform and stable BFM precursor solutions. However, the combinations of PVB + $Ca(NO_3)_2$ and PVP + $CaCl_2$ both possessed good compatibility between components, which could be applied for electrospinning. For PVP + $Ca(NO_3)_2$, the NO_3^- and PVP competed form hydrogen bond with chain-like polysiloxane (Fig. S1b). Therefore, the high concentration of NO_3^- would inhibit the formation of hydrogen bond of PVP, which suppressed it dissolution, while $CaCl_2$ would not. Nevertheless, PVB itself could form hydrogen bond with NO_3^- and promote the PVB dissolution inversely (Fig. S1c). For PVB + $CaCl_2$, the PVB couldn't dissolute because of the lack of hydrogen bond forming.

The morphology of BFMs with different R values (Fig. 1a) and calcined at different temperatures (Fig. 1b) was imaged under SEM. As Fig. 1a shown, the change of fibers diameter was not obvious as the R increased, but some fibers (R = 1.8 and 2.4) underwent fracture and crack, owing to fact that the reduction of spinnability caused the deterioration of the mechanical properties. The continuity of the fiber could

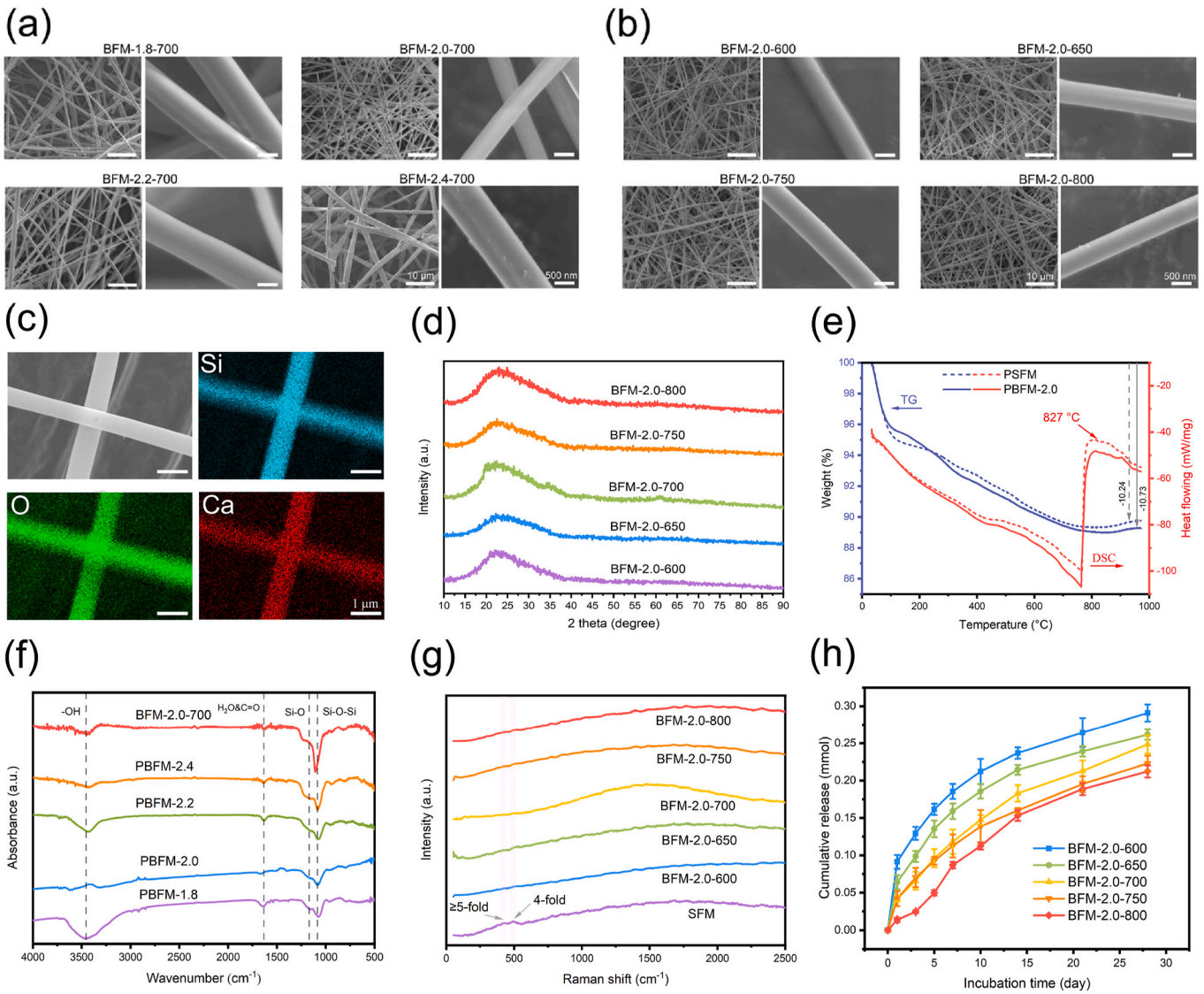

Fig. 1. Characterization of BFMs. (a) SEM images of BFMs with different R calcined at 700 °C. (b) SEM images of BFM at different calcination temperatures with R = 2.0. (c) EDS of BFM. (d) XRD of BFMs calcined at different temperatures with R = 2.0. (e) TG-DSC curves of PSFM and PBFM. (f) FTIR spectra of PBFMs with different R and BFM-2.0-700. (g) Raman spectra of SFM and BFMs at different calcination temperatures. (h) Cumulative Ca^{2+} release profile of BFMs during 28 days.

be well retained at different calcination temperatures. The element mapping of BFM (Fig. 1c) displayed that the elements Si, Ca, O were distributed evenly within the fibers and the distribution signals resembled the contours of the corresponding fibers. According to the element composition quantitative analysis (Fig. S2), the elements Si, Ca, O had an approximate ratio at different calcination temperatures. There was a small amount of residual chlorine (about 1.2 %) in BFM-2.0-600. This result implied that the calcination temperature need to exceed 600 °C to eliminate chlorine.

The XRD patterns of BFMs at different temperatures were shown in Fig. 1d. All samples exhibited typical amorphous halos, which indicated that BFMs did not be devitrified calcined at 800 °C. While the temperature exceeded 800 °C, the crystalline phase which was identified as calcium silicate (CS) occurred in BFM (Fig. S3a). The BFM calcined at 850 °C became brittle, which was easy to be broken and cannot be operated and tested (Fig. S3c), while calcined at 800 °C could keep flexibility and high-strength (Fig. S3b). Based on the above two reasons, the calcination temperature was set between 600 and 800 °C. According to TG curves (Fig. 1e), the first significant weight loss occurred near 120 °C, which was mainly attributed to the evaporation of small molecular solvents such as C_2H_5OH and H_2O. The second weight loss continued up to about 800 °C due to further polycondensation of Si-OH and decomposition of organic matter. The weight loss during calcination of PBFM was close to that of PSFM, which proved the PVP content in the PBFM was very low. This result was in accordance with the preparation method. The BFM with high density and good mechanical property could be obtained on account of fewer defect and porosity. A distinct exothermic peak appeared near 827 °C in DSC curves which implied a phase change near this temperature. The XRD of PBFM calcined at 850 °C (Fig. S3a) confirmed this result that BFM transition from amorphous phase to crystalline phase calcium silicate. The formed crystalline grains (calcium silicate crystals) caused the formation of cracks and fractures, hence damaging the flexibility and strength of BFM [29,30].

3.2. Atom state and chemical structure analysis

Fig. 1f illustrated the FTIR spectra for PBFMs and BFM-2.0-700 to explore the process of hydrolysis-polycondensation. The FTIR spectra for all samples showed a peak at 1660 cm^{-1}, which could be attributed to the overlap of the carbonyl stretching vibration of PVP and the bending vibration of absorbed water [31]. The peak at 1153 cm^{-1} gradually broadened from PBFM-1.8 to PBFM-2.4, indicating the

extension of the Si-O network and promotion of polycondensation [32]. This was in agreement with the fact that the amount of H_2O increased from PBFM-1.8 to PBFM-2.4. In addition, the increased intensity of the peak at 1082 cm^{-1} assigned to the asymmetrical stretching vibration of Si–O–Si was observed after calcination, implying the removal of the organic content and further polycondensation [33]. The peak at 3400 cm^{-1} belonging to –OH stretching vibration was present for all samples [34]. Thus, according to the FTIR results, the larger amount of H_2O promotes the polycondensation of Si-O network, which largely affected the spinnability. Low degree of polycondensation means insufficient entanglement between the chain-like polysiloxane for retaining the continuity of electrospinning jet, while overly high degree of polycondensation led to the reduction of spinnability owing to the structure conversion from Si–O linear chains to 3D network.

The BG network structure was explored by Raman spectra (Fig. 1g). Compared with SFM, the peaks at 423 and 495 cm^{-1} disappeared. The peaks at 423 and 495 cm^{-1} were ascribed to breathing modes of ⩾5 and 4 membered rings of [SiO_4], respectively [35]. Hence, the result demonstrated that the Ca^{2+} disrupted the continuity of the glass network, leading to the formation of non-bridging silicon–oxygen bonds (Si–O–NBO).What's more, the ATR-FTIR spectra (Fig. S4a) also confirmed the vitreous SiO_2 network destroy (decrease of Si-O-Si bond intensity) and creation of the local defects (peak of Si–O–NBO bond) [36]. And the higher calcination temperature led to the lower Si-O-Si bond intensity and the higher Si–O–NBO bond intensity. In addition, the XPS high-resolution peaks for Ca 2p was tested to investigated the chemical state of Ca (Fig. S4b). The Ca $2p_{3/2}$ peak was located at 347.47 eV, which was significantly different from its peak in $CaCl_2$ (348 eV) and CaO (346.6 eV) [37]. This implied that Ca didn't exist individually, but generated a certain connection with the SiO_2 network. Assessment of Ca^{2+} release was conducted for 28 days (Fig. 1h and Fig. S5). The Ca^{2+} release decreased with the increase of calcination temperature, indicating that the higher temperature, higher density of BG fiber. The higher calcination temperature was more conducive to the slower release of Ca^{2+}. Compared to 3D bioceramic scaffolds [38,39], BFM exhibited a significantly larger specific surface area, facilitating more intimate contact with bodily fluids and accelerating the release rate of ions such as Ca^{2+}. This enhanced ion release promoted the differentiation of osteoblasts more effectively.

3.3. Mechanical properties of BFMs

The mechanical properties of flexible nanofiber membranes are important for their practical application. However, as far as we know, no studies on the tensile strength of BFM have been reported up to now. To quantitatively evaluate the mechanical properties of the BFMs, tensile strength tests were conducted. As shown in Fig. 2a, the tensile strength values at 700 °C were 1.30, 2.31, 1.47 and 0.12 MPa for R = 1.8–2.4, respectively. According to previous analysis, too low water content couldn't generate enough condensation to prevent jet break up leading to fiber fracture, hence leading a lot amount short fibers in BFM-1.8-700, as shown in Fig. 1a. As for BFM-2.4-700, the high water content induced a large amount of hydrolyzed alkoxy groups and excessive condensation of silicon monomers, leading to transition from chain to non-chain or network polysiloxane and consequently reduction of spinnability. The obtained fiber represented significant fracture and the decline of continuity, which was in correspondence with SEM result. Alkoxysilane sol with high water content usually exhibits less spinnability and gel into elastic bulk masses that are easily converted to porous bulk glass. The fibers defect and fracture of BFM-2.4-700 likely resulted in severe degradation of mechanical performance. The influence of calcination temperature on tensile strength was illustrated in Fig. 2b. The tensile strengths obtained at 600–800 °C were 1.19, 1.27, 2.31, 1.57 and 0.94 MPa, respectively. Generally, the density of ceramic fibers increased with the elevation of calcination temperature. The decrease of tensile strength from 700 to 800 °C was possibly due to the micro crystal within the BG fibers, which couldn't be detected by XRD. To evaluate the flexibility of BFMs, the bending rigidity of samples with different R values were tested as shown in Fig. 2c. The result displayed that BFM-2.0-700 and BFM-2.2-700 were slightly higher than BFM-1.8-700 and BFM-2.4-700. Due to the existence of many short fibers in BFM-1.8-700 and BFM-2.4-700, the friction and entanglement between fibers receded a lot contributing to fiber fast slide. As for BFM-2.0-700 and BFM-2.2-700, BFM-2.0-700 possessed better density and less porosity, hence exhibiting better tensile strength and similar flexibility. According to the above analysis, BFM-2.0-700 displayed the best tensile strength due to good spin ability and nice density. As shown in Fig. S6, the tensile strength of BFM would decrease steadily from 2.07 MPa to 0.94 MPa with degradation of 28 days. This indicated that BFM could still maintaining a certain strength and stability to support bone tissue regeneration while releasing inorganic ions to promote osteogenic differentiation.

Medeiros et al. [40] produced a BG nanofibrous scaffolds by one-step solution blow spinning (SBS) process. Barros et al. [41] prepared a 3D fibrous structure of ICIE16 BG by air-heated solution blow spinning (A-HSBS). These researches of preparing BG fiber by SBS method obtained a 3D "cotton-wool" fibrous scaffold rather than 2D fiber membranes scaffold. Yuan et al. [42] prepared PVP-BG fibers (PVP content up to 50 %) with sol-gel process and converted electrospun PVP-BG fibers into short BG fibers through calcination and homogenization. The short BG fibers were used to fabricate aerogel scaffolds by blending the appropriate proportions including gelatin and dopamine. Yücel et al. [43] prepared a polyvinyl alcohol (PVA)-based nanofibrous membranes containing prepared nano-sized 45S5 BG particles loaded with chlorhexidine gluconate. Because of the limitation of the procedure of ES, the maximum load capacity of the 45S5 BG was only 5 %. Mahmoudi et al. [44] prepared a biocompatible fibrous scaffold containing PVA, 70S30C BG, silver (Ag) nanoparticles and curcumin (Cur) through ES method. The 70S30C BG was introduced into fibers in the form of sol and wasn't calcined, which could be degraded easily from the fibers after contact with body fluid.

Based on the above previous researches, without polymers binder, only short fiber could be obtained with any spinning method. However, only depending on the spinnablity of the polymer binder and adding sufficient amount to the system, the mechanical property of fiber would deteriorate after calcination and couldn't be used as self-supported fibers membranes. In addition, the introduction of BG in any form (particle or sol) as organic-inorganic composite fiber also had vital defects (lower loading content or too fast degradation). Therefore, the spinnability of the BG sol could be greatly improved by utilizing the alkoxysilane hydrolysis-condensation under an appropriate condition in this work. Therefore, the amount of polymer added can be significantly reduced, which greatly minimized the defects in the fibers caused by polymer removal during calcination. This improvement increases the density of the fibers, resulting in flexible and high-strength BFM.

3.4. Biomineralization experiments of BFMs

Fig. 2d showed the SEM images of BFMs with different calcination temperatures after soaking in SBF. After incubation of BFMs for 3 days, some cauliflower-like HCA particles were deposited on the fibers calcined at low temperatures (600 and 650 °C), while the other samples just generated part fibers break up. When incubated for 5 days, large degree of biomineralization occurred for BFM- 2.0-600, 650 and less for BFM-2.0-700, 750, with the fibers coated with a layer of HCA. The deposited cauliflower-like HCA particles grew and expanded further. After 7 days of soaking, the former 4 samples displayed that the fibers originally covered by HCA particles were devoured by newly deposited HCA, while BFM-2.0-800 showed no any obvious mineralization all the time. Fig. 2e showed the FTIR spectra of BFMs calcined at 600–800 °C after soaking in SBF for 7 days, and some new peaks associated with deposited biomineralization matter appeared. The double bands at

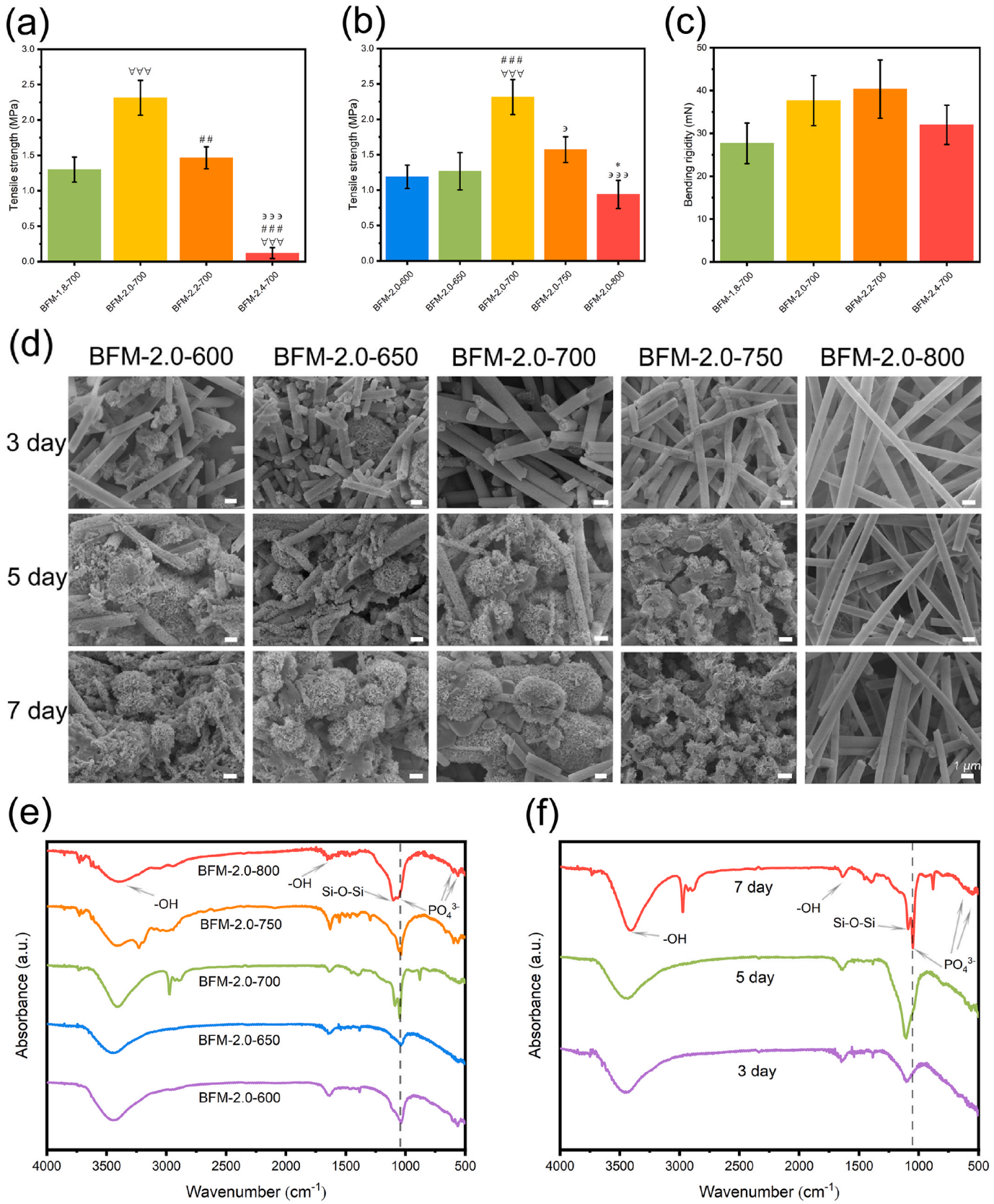

Fig. 2. Mechanical properties and biomineralization of BFMs. (a) Tensile strength of BFMs with different R at 700 °C. (b) Tensile strength of BFMs at different calcination temperatures with R = 2.0. (c) Bending rigidity of BFMs with different R calcined at 700 °C. (d) SEM images of BFMs after immersion in SBF for 3, 5 and 7 days. (e) FTIR spectra of BFMs at different calcination temperature after immersion in SBF for 7 days. (f) FTIR spectra of BFM-2.0-700 after immersion in SBF for different time.

about 560 and 600 cm^{-1} were assigned to the P-O bond bending vibrations, while the peak at 1040 cm^{-1} was ascribed to the P-O bond stretching vibrations [45]. The peak at 1040 cm^{-1} was reduced and covered by the characteristic band of Si-O-Si as the calcination temperature rose from 600 to 800 °C. The result implied that higher calcination temperature led to lower degree of biomineralization, in accordance with the SEM results. Higher calcination temperatures led to higher densities, which was unfavorable for biomineralization since enough surface energy (roughness) was required. BFM-2.0-700 was selected to study the influence of soaking time on biomineralization

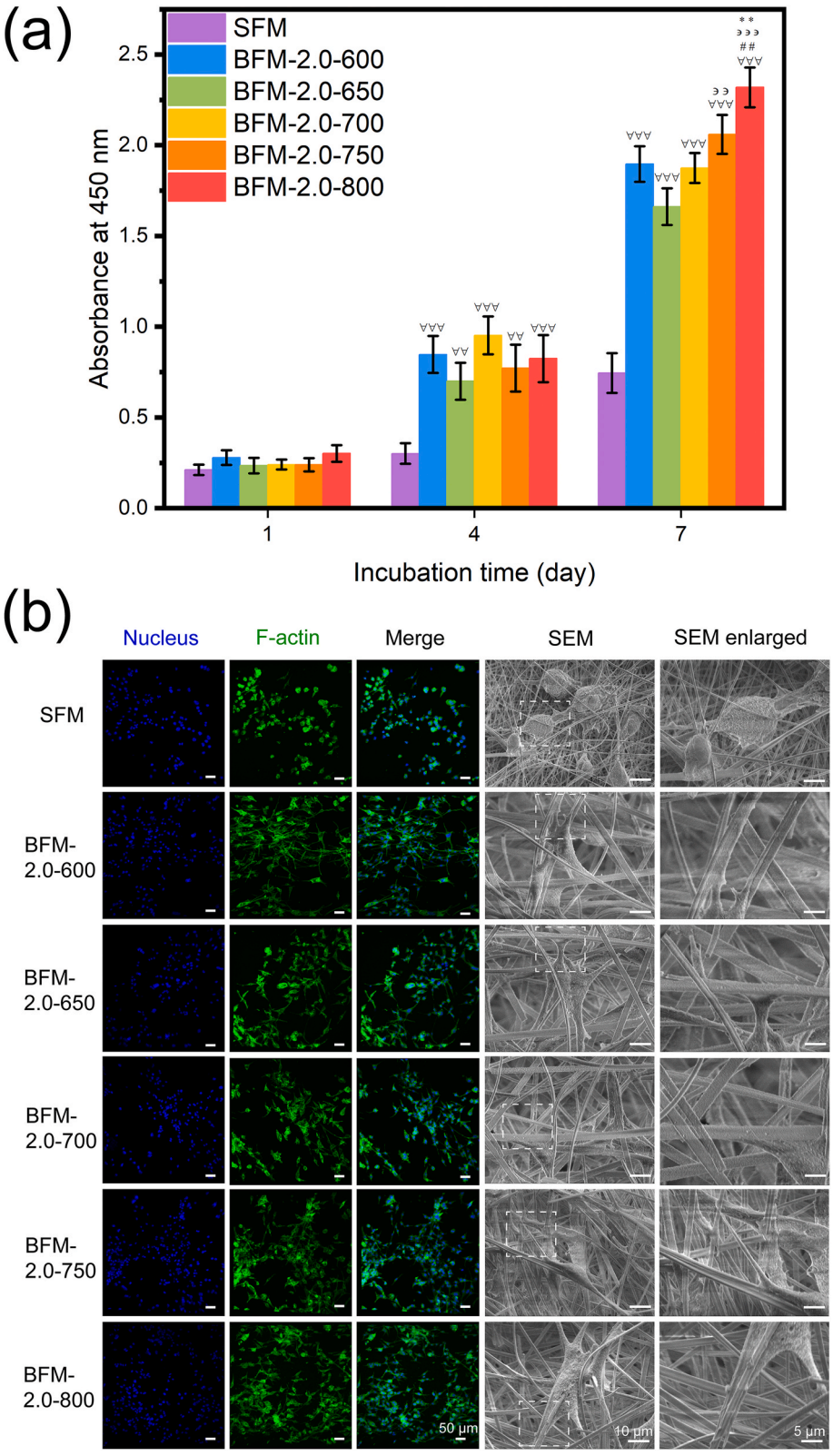

Fig. 3. Cell viability of MC3T3-E1 on BFMs. (a) Proliferation of MC3T3-E1 growing on SFM and BFMs calcined at 600–800 °C after 1, 4, and 7 days of incubation. (b) Adhesion and morphology of MC3T3-E1 growing on SFM and BFMs.

(Fig. 2f). A weak and broad FTIR band belonging to P-O was observed when incubated for 3 days, while the distinct band of P-O bond at 1040 cm^{-1} was obtained after 7 days of soaking. According to the SEM images and FTIR spectra, biominerazation *in vitro* decreased as the calcination temperature increased, and BFMs calcined at 600, 650, 700 and 750 °C could be deposited with crystalline HCA in a short time. In comparison to 3D bioceramic scaffolds [46], BFM offered a more extensive specific surface area and porosity, resulting in a faster release rate of Ca^{2+}. This enhanced the availability of surface sites and pH conditions conducive to HCA crystal nucleation, thereby significantly improving mineralization performance.

3.5. Cell adhesion and proliferation on BFMs

Heat treatment has a direct impact on BFM degradation and ion dissolution, determining the bone repair progress and osteogenesis healing time. On the other hand, the heat treatment could cause a terrific amount of cost due to very slow heating rate (1 °C/min) and long holding time (5 h), so finding an appropriate calcination temperature is quite necessary. As shown in Fig. 3a, as the culture time increased, the OD value of all samples increased persistently. The BFMs were far ahead of the SFM, displaying great performance of promoting cell proliferation. At the 1-day point, there were few difference between these samples because of a small amount of cells. By day 4, BFMs demonstrated a significant enhancement in MC3T3-E1 cell proliferation compared to SFM. This indicated that BFMs provided better support for cell adhesion and further promoted cell growth compared to SFM. However, no statistically significant differences were observed among the various BFMs groups, suggesting that the released Ca^{2+} concentrations across all groups remained within a cell-compatible range and that there was no apparent dose-dependent effect on cell proliferation. With higher calcination temperature, the BFMs degraded slower as well as fewer dissolved ion, as shown in Fig. 1h. At the point of the 7-day, there was a growing trend from BFM-2.0-650 to BFM-2.0-800. This indicated that BFM slower degradation and ions release became the more important factor of supporting cell growing for long time cell culture *in vitro*. The Calcein AM staining (Fig. S7) conformed the CCK-8 result. The living cells marked with Calcein AM (green) increased apparently as the culturing time increased. At point of the 4 days, BFM-2.0-700 demonstrated the maximum living cells, which was in coincidence with CCK-8 result.

The morphology of MC3T3-E1 revealed spindle-like shapes on BFMs and polygon or round-like on SFM (Fig. 3b). There were more extended pseudopodia of MC3T3-E1 to spread and adhere the BFMs fibers (SEM images enlarged). The cation exchange of BG fibers increased surface energy, hence adsorbing more ECM proteins (fibronectin, lamin) [47]. Consequently, more cellular receptors can bind to the adsorbed proteins leading to numerous focal adhesive sites enhancing cell adhesion [48,49]. On contrary, SFM wasn't suitable for cell spread and adhesion because of its relatively low dissolution rate and little adsorbed protein. However, no significant differences on cell morphologies between these BFMs at different calcination temperatures. This demonstrated that heat treatment temperature didn't have a significant impact on cell adhesion. In addition, due to the lack of through-holes smaller than 100 μm, 3D bioceramic scaffolds cannot effectively guide cells to extend and grow inside the scaffolds [50,51]. In contrast, MC3T3-E1 cells were able to adhere along BFM fibers and migrate continuously into the scaffold through the interstitial spaces between the fibers (Fig. 3b SEM).

3.6. Cell osteogenic differentiation on BFMs

To evaluate the effect of heat treatment on osteogenic differentiation, RT-PCR was employed to evaluate it at the mRNA level by detecting 4 osteogenic –related genes, including *RUNX2*, *ALP*, *COL1* and *OCN*. In Fig. 4a, the expression level of *RUNX2* in BFM-2.0-750 was obviously higher than other group, and all BFMs were higher than SFM. *RUNX2* is a representative gene at early stage of osteogenic differentiation, which works as a transcription factor to activate the expression of

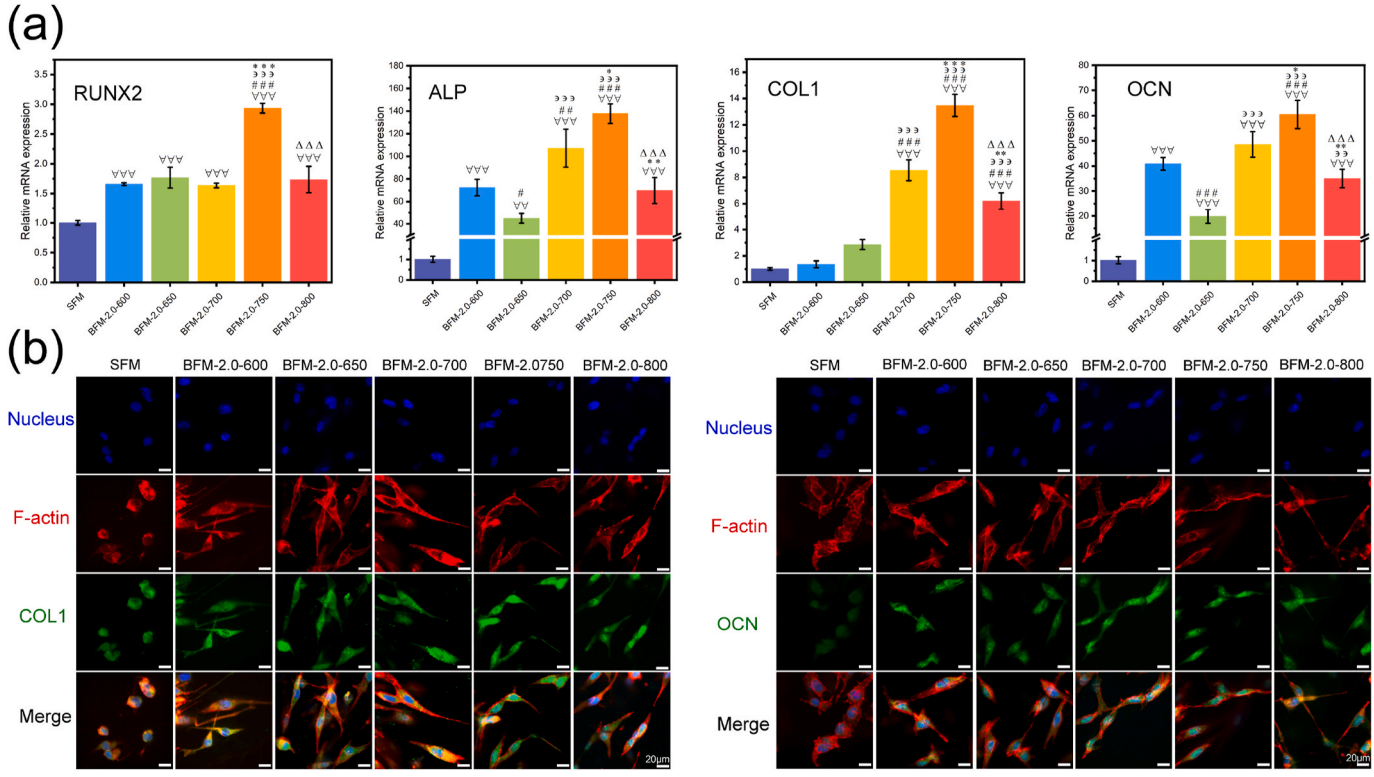

Fig. 4. Osteogenic differentiation of MC3T3-E1 growing on BFMs. (a) Relative genes expression level of MC3T3-E1 growing on SFM and BFMs. (b) IF staining of COL1 and OCN of MC3T3-E1 growing on SFM and BFMs.

downstream osteogenic-related genes. *ALP* is a hallmark enzyme of osteoblast differentiation, which is involved in the regulation of calcification and promote mineral deposition in bone tissue, also expressing at early stage. BFMs exhibited a very huge promotion in *ALP* expression compared to SFM. And BFM-2.0-750 displayed a higher expression among these BFMs groups. Presumably, a moderate and continuous dissolution of Ca^{2+} could stimulate the expression of *ALP*. Too fast (BFM-2.0-600 and 650) and slow (BFM-2.0-800) dissolution rate couldn't effectively promote it either. *COL1* is a major component of the extracellular matrix, which provides a template for the deposition of bone minerals, as a prerequisite for bone tissue formation. The expression of *COL1* increased from BFM-2.0-600 to BFM-2.0-750 and reached the highest in BFM-2.0-750 group. It also indicated that relatively low degradation rate was more beneficial to *COL1* expression. *OCN* is a marker of advanced osteogenesis, a regulator of bone mineral formation and growth, and increases until the mineralization stage. The expression of *OCN* showed a similar trend with *ALP*. Consequently, the higher *ALP* expression in BFM-2.0-750 perhaps facilitated the *OCN* expression.

The COL1 and OCN were selected as the remarkable osteogenic proteins indicators to investigated the osteogenesis expression via IF staining. From the IF images and quantitative analyses (Fig. 4b and Fig. S8), the BFM-2.0-750 displayed enhanced expression of COL1 and OCN, which were accordant with PCR result. The COL1 expression rose from BFM-2.0-600 to BFM-2.0-750 and declined in BFM-2.0-800 group. As for OCN, BFM-2.0-750 displayed a higher expression among these BFMs groups. This may be due to the fact that more sustained and slower release of Ca^{2+} is more conducive to the expression of OCN. Based on above results, all BFMs possessed great performance of supporting osteogenic differentiation in comparison with SFM. Higher calcination temperature (700–750 °C) greatly improved the MC3T3-E1 osteogenic

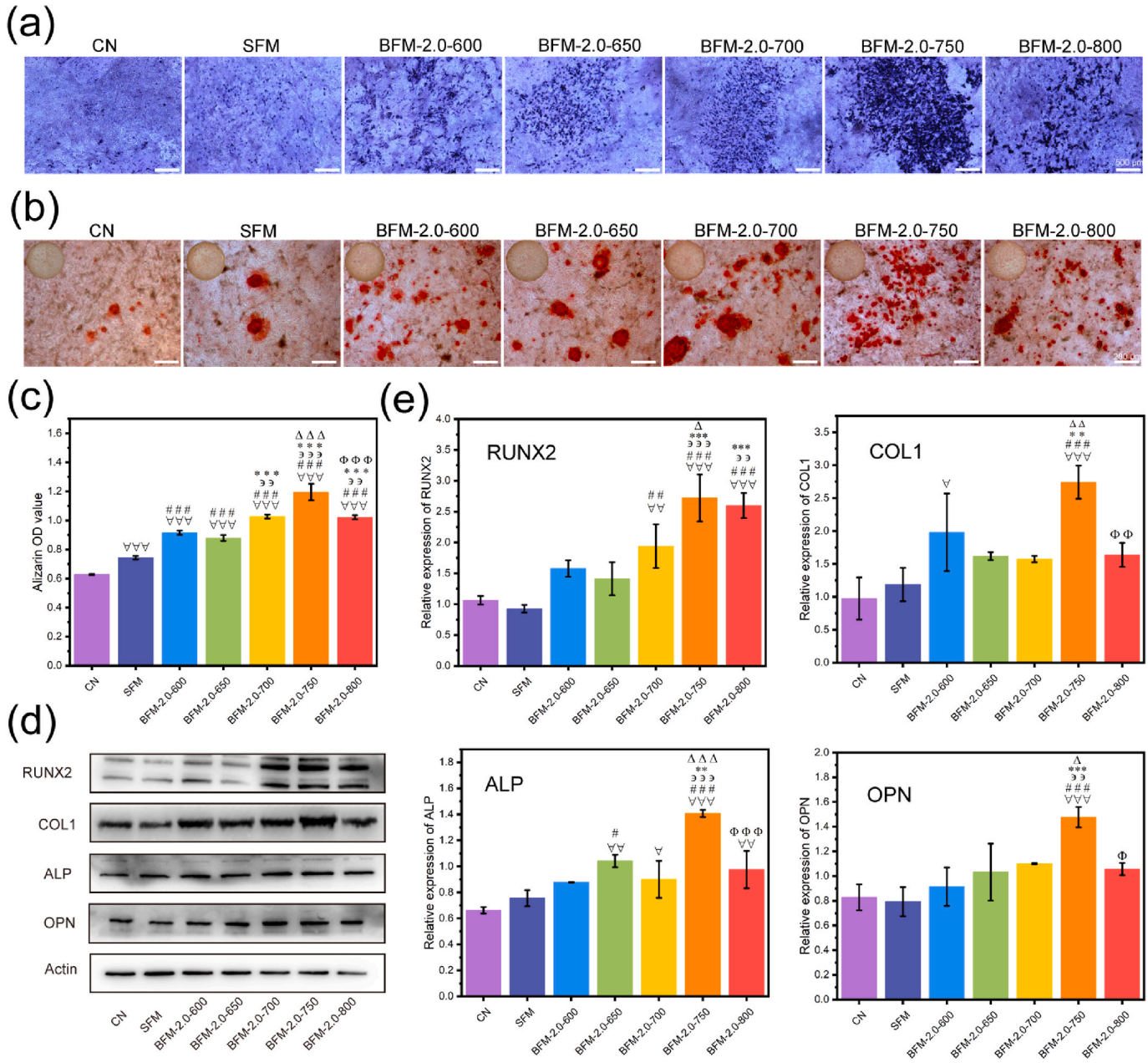

Fig. 5. Osteogenic differentiation of MC3T3-E1 with SFM and BFMs leach liquor. (a) ALP staining of MC3T3-E1 cultured with SFM and BFMs leach liquor. (b) ARS staining of MC3T3-E1 cultured with SFM and BFMs leach liquor. (c) Quantitative analysis of ARS staining. (d) WB assays of MC3T3-E1 cultured with SFM and BFMs leach liquor. (e) Quantitative analysis of WB assays.

differentiation performance on BFMs, especially 750 °C.

3.7. Cell osteogenic differentiation with BFMs leach liquor

According to ALP and ARS staining and the quantitative analyses (Fig. 5a–c), all the BFMs revealed good osteogenic differentiation and mineralization ability, compared to SFM and the CN. In general, higher calcination temperature (700–750 °C) implied better osteogenic differentiation performance and BFM-2.0-750 was the best, which was consistent with osteogenic differentiation of MC3T3-E1 growing on BFMs.

Four osteogenesis-related proteins were detected by Western bloting and their relative protein expression levels were evaluated, including COL1, RUNX2, OPN, ALP (Fig. 5d and e). The expression levels of these four proteins were similar to the results of RT-PCR, and the expression levels were higher in the BFM-2.0-750 group. The above results *in vitro* indicated that higher calcination temperatures led to longer ion release and degradation times, thus favoring prolonged osteogenic differentiation processes.

3.8. BFMs in vivo studies

The performance of BFM promoting osteogenesis was also verified by animal experiment. After 8-week implantation, rat skull samples were extracted and evaluated by Micro-CT. Within 8 weeks, the BFM-2.0-750 group showed more regeneration of new bone, with the most reconstruction of bone defects in the area. These results were further quantified by calculating BV/TV, TB.N and BMD at 8 week (Fig. 6b–d), which were consistent with the Micro-CT results. The BFM-2.0-750 group had the highest values for each. This was owing that BFM could provide mechanical and spatial support for cell growth and promote proliferation and differentiation.

Tissue sections HE and Masson staining were shown in Fig. 7a and b. After 8 weeks of *in vivo* implantation, only connective tissue regeneration with little bone formation was observed in the CN and SFM groups, whereas new bone tissue regeneration was observed in the BFM-2.0-750 group. The highest amount of bone regeneration was in the BFM-2.0-750 group, which was superior to the SFM group (Fig. 7b), as reflected in the more mature and thicker new bone. *In vivo* immunohistochemistry showed that the positive expression of OCN and ALP (Fig. 7c–e) in the BFM-2.0-750 group was much larger than that in the other two groups, which could also indicate that the BFM-2.0-750 group had a stronger

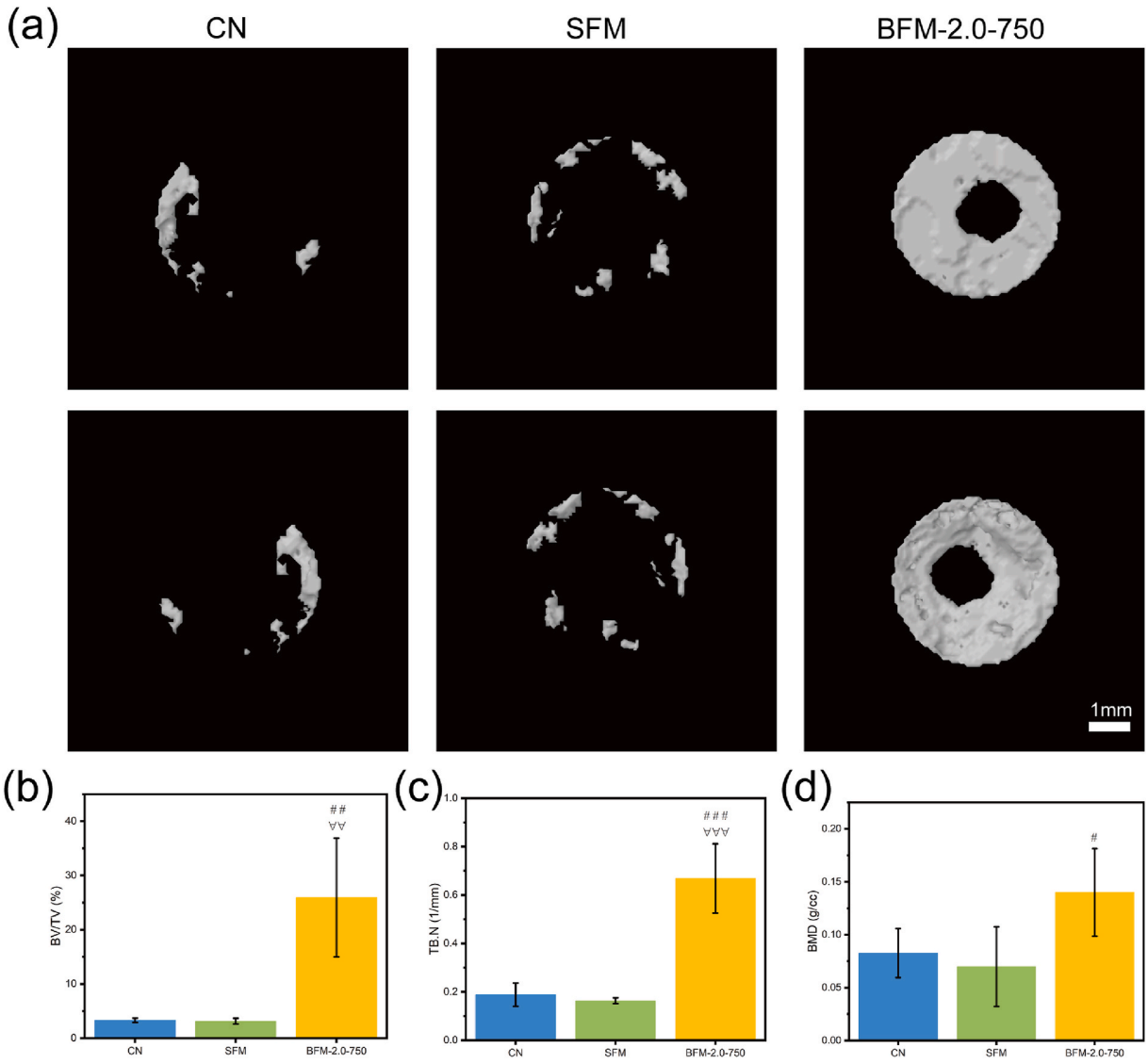

Fig. 6. Micro-CT evaluation of bone repair post-implantation in skull defect model at 8 week. (a) Micro-CT evaluation and (b–d) quantitative analysis of BV/TV, TB.N and BMD within harvested samples.

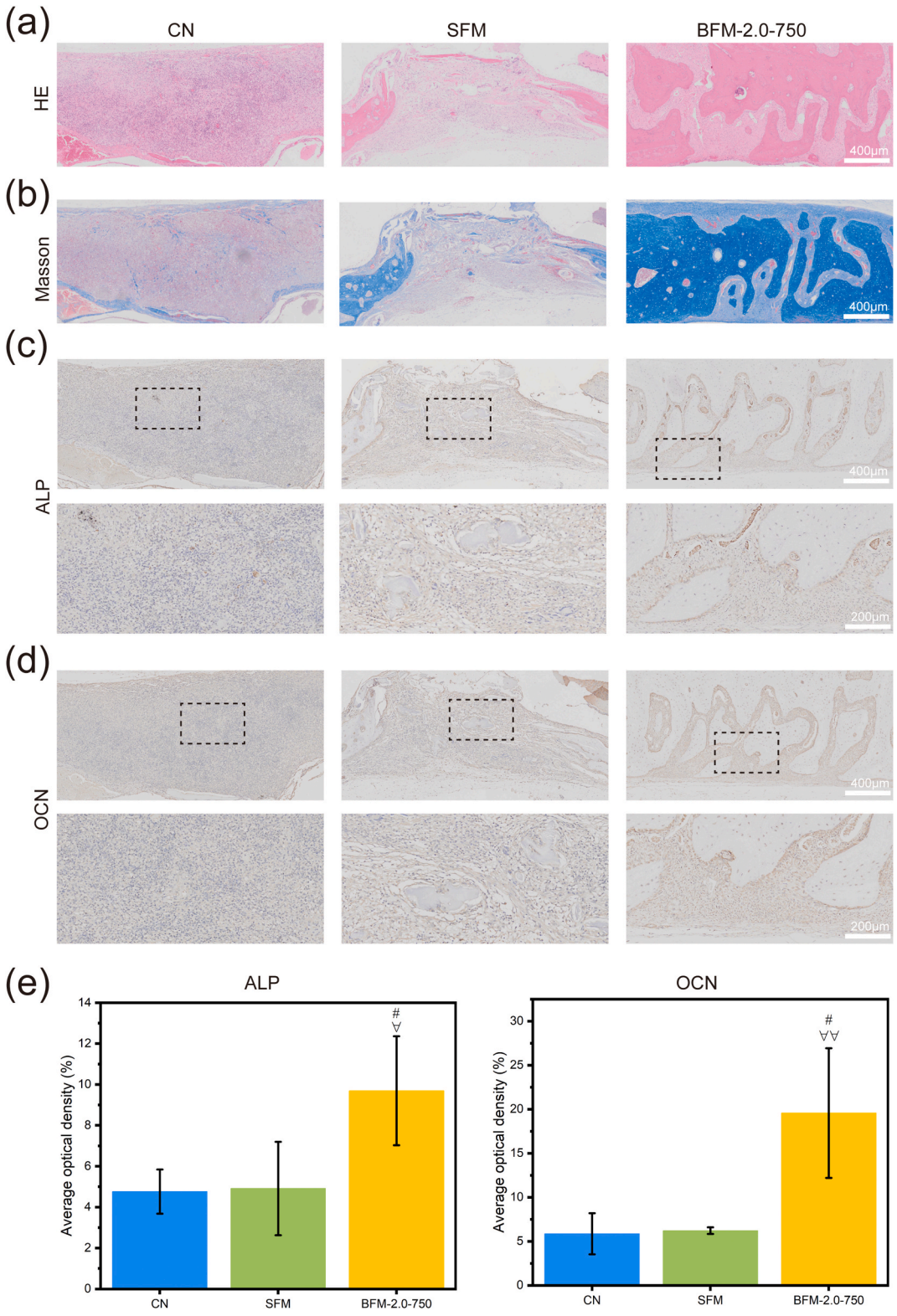

Fig. 7. Histological and immunohistochemistry images *in vivo*. (a) HE of rat skulls in different groups. (b) Masson of rat skulls of different groups. (c, d) IHC analysis of ALP and OCN of different groups (IHC positive: brown). (e) Quantitative analysis of ALP and OCN of different groups. (For interpretation of the references to color in this figure legend, the reader is referred to the Web version of this article.)

osteogenic ability.

4. Conclusion

In summary, the electrospun BFM with minute quantity polymer binder was developed, combining the spinnability of alkoxysilane sol with specific condition and polymer binder. The effect of R was investigated particularly. When R was 2.0, the obtained BFM possessed best tensile strength and great flexibility. The BFM could remain good mechanical performance from 600 to 800 °C. In cell study, all BFM

demonstrated great cell adhesion and morphology. The CCK-8 result revealed that the higher calcination temperature could support cell proliferation better. Similarly, the BFM calcined at higher temperature (especially 750 °C) possessed a better promoting effect on osteogenic differentiation. The BFM calcined at 750 °C was selected to be inspected with rat skull defect models, demonstrating a good effect on osteogenesis *in vivo*. So to sum up, the BFM obtained from independent-polymer binder electrospinning not only possessed great mechanical performance and practicability, but also exhibited good bone tissue regeneration potential.

CRediT authorship contribution statement

Junjie Mao: Writing – review & editing, Writing – original draft, Supervision, Software, Resources, Methodology, Investigation, Formal analysis, Data curation. **Junyuan Sun:** Writing – review & editing, Writing – original draft, Methodology, Investigation, Formal analysis, Data curation. **Lu Wang:** Supervision, Software, Resources, Methodology, Investigation. **Xinyu Liu:** Visualization, Validation, Supervision, Resources, Investigation, Funding acquisition. **Jianqiang Bi:** Visualization, Validation, Supervision, Software, Resources, Methodology, Investigation, Funding acquisition.

Declaration of competing interest

The authors declare that they have no known competing financial interests or personal relationships that could have appeared to influence the work reported in this paper.

Data availability

The data that has been used is confidential.

Acknowledgements

This work was supported by Key R&D Program of Shandong Province (2023CXGC010305), the Special Fund for Leading Talent in Mount Tai of Shandong Province, the National Nature Science Foundation (81874022, 82172483 and 82102522), Shandong Province Taishan Scholar Project (tstp20231247), Key R&D Project of Shandong Province (2022CXGC010503), Shandong Natural Science Foundation (ZR202102210113) and National High Level Hospital Clinical Research Funding (2022-PUMCH-D-004)

Appendix A. Supplementary data

Supplementary data to this article can be found online at https://doi.org/10.1016/j.mtbio.2024.101224.

References

[1] M. Vallet-Regi, E. Ruiz-Hernandez, Bioceramics: from bone regeneration to cancer nanomedicine, Adv Mater 23 (2011) 5177–5218, https://doi.org/10.1002/adma.201101586.

[2] T. Guo, M. Noshin, H.B. Baker, E. Taskoy, S.J. Meredith, Q. Tang, J.P. Ringel, M. J. Lerman, Y. Chen, J.D. Packer, J.P. Fisher, 3D printed biofunctionalized scaffolds for microfracture repair of cartilage defects, Biomaterials 185 (2018) 219–231, https://doi.org/10.1016/j.biomaterials.2018.09.022.

[3] G. Turnbull, J. Clarke, F. Picard, P. Riches, L. Jia, F. Han, B. Li, W. Shu, 3D bioactive composite scaffolds for bone tissue engineering, Bioact. Mater. 3 (2018) 278–314, https://doi.org/10.1016/j.bioactmat.2017.10.001.

[4] S. Pina, J.M. Oliveira, R.L. Reis, Natural-based nanocomposites for bone tissue engineering and regenerative medicine: a review, Adv Mater 27 (2015) 1143–1169, https://doi.org/10.1002/adma.201403354.

[5] Q. Fu, E. Saiz, M.N. Rahaman, A.P. Tomsia, Toward strong and tough glass and ceramic scaffolds for bone repair, Adv. Funct. Mater. 23 (2013) 5461–5476, https://doi.org/10.1002/adfm.201301121.

[6] A.A. White, S.M. Best, I.A. Kinloch, Hydroxyapatite–carbon nanotube composites for biomedical applications: a review, Int. J. Appl. Ceram. Technol. 4 (2007) 1–13, https://doi.org/10.1111/j.1744-7402.2007.02113.x.

[7] J.W. Lee, B. Lee, C.H. Park, J.H. Heo, T.Y. Lee, D. Lee, J. Bae, P.R. Sundharbaabu, W.K. Yeom, S. Chae, J.-H. Lim, S.-W. Lee, J.-S. Choi, H.-B. Bae, J.-Y. Choi, E.-H. Lee, D.S. Yoon, G.Y. Yeom, H. Shin, J.H. Lee, Monolithic DNApatite: an elastic apatite with sub-nanometer scale organo–inorganic structures, Adv. Mater. n/a (2024) 2406179, https://doi.org/10.1002/adma.202406179.

[8] M.A. Lopes, F.J. Monteiro, J.D. Santos, Glass-reinforced hydroxyapatite composites: fracture toughness and hardness dependence on microstructural characteristics, Biomaterials 20 (1999) 2085–2090, https://doi.org/10.1016/S0142-9612(99)00112-X.

[9] G. Chen, Y. Sun, F. Lu, A. Jiang, D. Subedi, P. Kong, X. Wang, T. Yu, H. Chi, C. Song, K. Liu, P. Qi, J. Yan, Y. Ji, A three-dimensional (3D) printed biomimetic hierarchical scaffold with a covalent modular release system for osteogenesis, Mater. Sci. Eng. C 104 (2019) 109842, https://doi.org/10.1016/j.msec.2019.109842.

[10] Q. Nawaz, A. de Pablos-Martín, A.T. Contreras Jaimes, F. Scheffler, T. Wagner, D. S. Brauer, A.R. Boccaccini, Comparison of microstructure, sintering behavior, and biological response of sol-gel and melt-derived 13–93 bioactive glass scaffolds, Open Ceramics 15 (2023) 100407, https://doi.org/10.1016/j.oceram.2023.100407.

[11] Y. Peng, M. Chen, J. Wang, J. Xie, C. Wang, X. Yang, X. Huang, Z. Gou, J. Ye, Tuning zinc content in wollastonite bioceramic endowing outstanding angiogenic and antibacterial functions beneficial for orbital reconstruction, Bioact. Mater. 36 (2024) 551–564, https://doi.org/10.1016/j.bioactmat.2024.02.027.

[12] M. Nagrath, A. Alhalawani, A. Rahimnejad Yazdi, M.R. Towler, Bioactive glass fiber fabrication via a combination of sol-gel process with electro-spinning technique, Mater. Sci. Eng., C 101 (2019) 521–538, https://doi.org/10.1016/j.msec.2019.04.003.

[13] Y. Xu, W. Cui, Y. Zhang, P. Zhou, Y. Gu, X. Shen, B. Li, L. Chen, Hierarchical micro/nanofibrous bioscaffolds for structural tissue regeneration, Adv. Healthcare Mater. 6 (2017) 1601457, https://doi.org/10.1002/adhm.201601457.

[14] X. Fu, J. Wang, D. Qian, L. Xi, L. Chen, Y. Du, W. Cui, Y. Wang, Oxygen atom-concentrating short fibrous sponge regulates cellular respiration for wound healing, Adv Fiber Mater 5 (2023) 1773–1787, https://doi.org/10.1007/s42765-023-00310-7.

[15] Y. Sun, S. Cheng, W. Lu, Y. Wang, P. Zhang, Q. Yao, Electrospun fibers and their application in drug controlled release, biological dressings, tissue repair, and enzyme immobilization, RSC Adv. 9 (2019) 25712–25729, https://doi.org/10.1039/c9ra05012d.

[16] L. Weng, S.K. Boda, M.J. Teusink, F.D. Shuler, X. Li, J. Xie, Binary doping of strontium and copper enhancing osteogenesis and angiogenesis of bioactive glass nanofibers while suppressing osteoclast activity, ACS Appl. Mater. Interfaces 9 (2017) 24484–24496, https://doi.org/10.1021/acsami.7b06521.

[17] J. Chen, S. Wan, Y. Fu, Y. Zhou, X. Li, H. Wang, An implantable composite scaffold for amplified chemodynamic therapy and tissue regeneration, J. Mater. Chem. B 11 (2023) 3151–3163, https://doi.org/10.1039/D2TB02699F.

[18] J. Li, Y. Zhang, X. Zhou, S. Wang, R. Hao, J. Han, M. Li, Y. Zhao, C. Chen, H. Xu, Enzymatically functionalized RGD-gelatin scaffolds that recruit host mesenchymal stem cells in vivo and promote bone regeneration, J. Colloid Interface Sci. 612 (2022) 377–391, https://doi.org/10.1016/j.jcis.2021.12.091.

[19] X. Liu, M. Chen, J. Luo, H. Zhao, X. Zhou, Q. Gu, H. Yang, X. Zhu, W. Cui, Q. Shi, Immunopolarization-regulated 3D printed-electrospun fibrous scaffolds for bone regeneration, Biomaterials 276 (2021) 121037, https://doi.org/10.1016/j.biomaterials.2021.121037.

[20] J. Zhang, S. Li, D.-D. Ju, X. Li, J.-C. Zhang, X. Yan, Y.-Z. Long, F. Song, Flexible inorganic core-shell nanofibers endowed with tunable multicolor upconversion fluorescence for simultaneous monitoring dual drug delivery, Chem. Eng. J. 349 (2018) 554–561, https://doi.org/10.1016/j.cej.2018.05.112.

[21] S. Lin, C. Ionescu, K.J. Pike, M.E. Smith, J.R. Jones, Nanostructure evolution and calcium distribution in sol–gel derived bioactive glass, J. Mater. Chem. 19 (2009) 1276, https://doi.org/10.1039/b814292k.

[22] L.J. Skipper, F.E. Sowrey, D.M. Pickup, K.O. Drake, M.E. Smith, P. Saravanapavan, L.L. Hench, R.J. Newport, The structure of a bioactive calcia–silica sol–gel glass, J. Mater. Chem. 15 (2005) 2369, https://doi.org/10.1039/b501496d.

[23] S. Sakka, K. Kamiya, The sol-gel transition in the hydrolysis of metal alkoxides in relation to the formation of glass fibers and films, J. Non-Cryst. Solids 48 (1982) 31–46, https://doi.org/10.1016/0022-3093(82)90244-7.

[24] S. Sakka, Sol–gel technology as representative processing for nanomaterials: case studies on the starting solution, J. Sol. Gel Sci. Technol. 46 (2007) 241–249, https://doi.org/10.1007/s10971-007-1651-6.

[25] G. Poologasundarampillai, D. Wang, S. Li, J. Nakamura, R. Bradley, P.D. Lee, M. M. Stevens, D.S. McPhail, T. Kasuga, J.R. Jones, Cotton-wool-like bioactive glasses for bone regeneration, Acta Biomater. 10 (2014) 3733–3746, https://doi.org/10.1016/j.actbio.2014.05.020.

[26] Y. Xie, L. Wang, Y. Peng, D. Ma, L. Zhu, G. Zhang, X. Wang, High temperature and high strength $Y_2Zr_2O_7$ flexible fibrous membrane for efficient heat insulation and acoustic absorption, Chem. Eng. J. 416 (2021) 128994, https://doi.org/10.1016/j.cej.2021.128994.

[27] W. Han, F. Cui, Y. Si, X. Mao, B. Ding, H. Kim, Self-assembly of perovskite crystals anchored Al_2O_3 -La_2O_3 nanofibrous membranes with robust flexibility and luminescence, Small 14 (2018) e1801963, https://doi.org/10.1002/smll.201801963.

[28] T. Kokubo, H. Kushitani, S. Sakka, T. Kitsugi, T. Yamamuro, Solutions able to reproduce in vivo surface-structure changes in bioactive glass-ceramic A-W3, J. Biomed. Mater. Res. 24 (1990) 721–734, https://doi.org/10.1002/jbm.820240607.

[29] L. Wang, Y. Qiu, Y. Guo, Y. Si, L. Liu, J. Cao, J. Yu, X. Li, Q. Zhang, B. Ding, Smart, elastic, and nanofiber-based 3D scaffolds with self-deploying capability for osteoporotic bone regeneration, Nano Lett. 19 (2019) 9112–9120, https://doi.org/10.1021/acs.nanolett.9b04313.
[30] M. Liu, X. Wang, J. Cui, H. Wang, B. Sun, J. Zhang, B. Rolauffs, M. Shafiq, X. Mo, Z. Zhu, J. Wu, Electrospun flexible magnesium-doped silica bioactive glass nanofiber membranes with anti-inflammatory and pro-angiogenic effects for infected wounds, J. Mater. Chem. B 11 (2023) 359–376, https://doi.org/10.1039/d2tb02002e.
[31] G. Song, Z. Li, K. Li, L. Zhang, A. Meng, SiO_2/ZnO composite hollow sub-micron fibers: fabrication from facile single capillary electrospinning and their photoluminescence properties, Nanomaterials-Basel 7 (2017) 53, https://doi.org/10.3390/nano7030053.
[32] D. Niznansky, J.L. Rehspringer, Infrared study of SiO_2 sol to gel evolution and gel aging, J. Non-Cryst. Solids 180 (1995) 191–196, https://doi.org/10.1016/0022-3093(94)00484-6.
[33] F. Gao, Y. Song, Y. Sheng, C. Lin, Q. Huo, H. Zou, Growth, structure and optical properties of tartaric acid-templated silica nanotubes by sol–gel method, J. Sol. Gel Sci. Technol. 68 (2013) 204–212, https://doi.org/10.1007/s10971-013-3152-0.
[34] X. Zhao, Y. Zhuang, Y. Cao, F. Cai, Y. Lv, Y. Zheng, J. Yang, X. Shi, Electrospun biomimetic periosteum capable of controlled release of multiple agents for programmed promoting bone regeneration, Adv. Healthcare Mater. 13 (2024) 2303134, https://doi.org/10.1002/adhm.202303134.
[35] S.K. Sharma, J.F. Mammone, M.F. Nicol, Raman investigation of ring configurations in vitreous silica, Nature 292 (1981) 140–141, https://doi.org/10.1038/292140a0.
[36] S. Ben Khemis, E. Burov, H. Montigaud, D. Skrelic, E. Gouillart, L. Cormier, Structural analysis of sputtered amorphous silica thin films: a Raman spectroscopy investigation, Thin Solid Films 733 (2021) 138811, https://doi.org/10.1016/j.tsf.2021.138811.
[37] B. Demri, D. Muster, XPS study of some calcium compounds, J. Mater. Process. Technol. 55 (1995) 311–314, https://doi.org/10.1016/0924-0136(95)02023-3.
[38] H. Zhang, K. Han, L. Dong, X. Li, Preparation and characterization of β-tricalcium phosphate/nano clay composite scaffolds via digital light processing printing, J. Inorg. Mater. 37 (2022) 1116–1122, https://doi.org/10.15541/jim20210745.
[39] S.S. Chon, L. Piraino, S. Mokhtari, E.A. Krull, A. Coughlan, Y. Gong, N.P. Mellott, T. J. Keenan, A.W. Wren, Synthesis, characterization and solubility analysis of amorphous SiO_2-CaO-Na_2O-P_2O_5 scaffolds for hard tissue repair, J. Non-Cryst. Solids 490 (2018) 1–12, https://doi.org/10.1016/j.jnoncrysol.2018.03.006.
[40] E.L.G. Medeiros, D.S. Gomes, A.M.C. Santos, R.H. Vieira, I.L. de Lima, F.S. Rocha, L.d.S. Castro-Filice, E.S. Medeiros, G.A. Neves, R.R. Menezes, 3D nanofibrous bioactive glass scaffolds produced by one-step spinning process, Ceram. Int. 47 (2021) 102–110, https://doi.org/10.1016/j.ceramint.2020.08.112.
[41] L.N.L.C. Barros, V.C. Silva, R.N.d. Araujo, D.B. Silva, G.d.A. Neves, R.R. Menezes, Production of 3D fibrous structure of ICIE16 bioactive glass by air-heated solution blow spinning (A-HSBS), Mater. Lett. 365 (2024) 136440, https://doi.org/10.1016/j.matlet.2024.136440.
[42] Z. Yuan, L. Zhang, M. Shafiq, X. Wang, P. Cai, A. Hafeez, Y. Ding, Z. Wang, M. El-Newehy, A. Meera Moydeen, L. Jiang, X. Mo, Y. Xu, Composite superplastic aerogel scaffolds containing dopamine and bioactive glass-based fibers for skin and bone tissue regeneration, J. Colloid Interface Sci. 673 (2024) 411–425, https://doi.org/10.1016/j.jcis.2024.06.098.
[43] C. Keçeciler-Emir, Y. Başaran-Elalmiş, Y.M. Şahin, E. Buluş, S. Yücel, Fabrication and characterization of chlorhexidine gluconate loaded poly(vinyl alcohol)/45S5 nano-bioactive glass nanofibrous membrane for guided tissue regeneration applications, Biopolymers 114 (2023) e23562, https://doi.org/10.1002/bip.23562.
[44] M. Mahmoudi, P. Alizadeh, M. Soltani, Wound healing performance of electrospun PVA/70S30C bioactive glass/Ag nanoparticles mats decorated with curcumin: in vitro and in vivo investigations, Biomater. Adv. 153 (2023) 213530, https://doi.org/10.1016/j.bioadv.2023.213530.
[45] A.M. Deliormanli, Preparation, in vitro mineralization and osteoblast cell response of electrospun 13-93 bioactive glass nanofibers, Mater. Sci. Eng., C 53 (2015) 262–271, https://doi.org/10.1016/j.msec.2015.04.037.
[46] R. Lian, P. Xie, L. Xiao, Z. Iqbal, S. Zhang, J. Kohn, X. Qu, C. Liu, Y. Li, Rational design and fabrication of biomimetic hierarchical scaffolds with bone-matchable strength for bone regeneration, Frontiers in Materials 7 (2021), https://doi.org/10.3389/fmats.2020.622669.
[47] R. Ghobeira, C. Philips, L. Liefooghe, M. Verdonck, M. Asadian, P. Cools, H. Declercq, W.H. De Vos, N. De Geyter, R. Morent, Synergetic effect of electrospun PCL fiber size, orientation and plasma-modified surface chemistry on stem cell behavior, Appl. Surf. Sci. 485 (2019) 204–221, https://doi.org/10.1016/j.apsusc.2019.04.109.
[48] S. Metwally, S. Ferraris, S. Spriano, Z.J. Krysiak, Ł. Kaniuk, M.M. Marzec, S.K. Kim, P.K. Szewczyk, A. Gruszczyński, M. Wytrwal-Sarna, J.E. Karbowniczek, A. Bernasik, S. Kar-Narayan, U. Stachewicz, Surface potential and roughness controlled cell adhesion and collagen formation in electrospun PCL fibers for bone regeneration, Mater Dseign 194 (2020) 108915, https://doi.org/10.1016/j.matdes.2020.108915.
[49] Y.K. Fuh, Y.C. Wu, Z.Y. He, Z.M. Huang, W.W. Hu, The control of cell orientation using biodegradable alginate fibers fabricated by near-field electrospinning, Mater. Sci. Eng., C 62 (2016) 879–887, https://doi.org/10.1016/j.msec.2016.02.028.
[50] I. Won Suh, J. In Kim, B. Kumar Shrestha, S. Rim Jang, C. Hee Park, Flower-like Ti(HPO4)2 bioceramic-laden 3D printed platform for enhanced bone regeneration via BMP signaling pathway, Chem. Eng. J. 487 (2024) 150757, https://doi.org/10.1016/j.cej.2024.150757.
[51] G. Yang, C. Qin, J. Chen, Z. Yang, W. Ma, Z. Cao, X. Zhao, L. Chen, C. Wu, Q. Yao, Black bioceramic scaffolds with micro/nano surface structure inducing mild hyperthermal environment for regenerating osteochondral defects, Nano Today 57 (2024) 102387, https://doi.org/10.1016/j.nantod.2024.102387.